



# Lidar system with nonmechanical electrowetting-based wide-angle beam steering

MO ZOHRABI,<sup>1,\*</sup> WEI YANG LIM,<sup>2</sup> ROBERT H. CORMACK,<sup>1</sup> OMKAR D. SUPEKAR,<sup>2</sup> VICTOR M. BRIGHT,<sup>2</sup> AND JULIET T. GOPINATH<sup>1,3</sup>

<sup>1</sup>*Department of Electrical, Computer, and Energy Engineering, University of Colorado, Boulder, Colorado 80309, USA*

<sup>2</sup>*Department of Mechanical Engineering, University of Colorado Boulder, Colorado 80309, USA*

<sup>3</sup>*Department of Physics, University of Colorado, Boulder, Colorado 80309, USA*

\*[mo.zohrabi@colorado.edu](mailto:mo.zohrabi@colorado.edu)

**Abstract:** A light detection and ranging (lidar) system with  $\pm 90^\circ$  of steering based on an adaptive electrowetting-based prism for nonmechanical beam steering has been demonstrated. Electrowetting-based prisms provide a transmissive, low power, and compact alternative to conventional adaptive optics as a nonmechanical beam scanner. The electrowetting prism has a steering range of  $\pm 7.8^\circ$ . We demonstrate a method to amplify the scan angle to  $\pm 90^\circ$  and perform a one-dimensional scan in a lidar system.

© 2019 Optical Society of America under the terms of the [OSA Open Access Publishing Agreement](#)

## 1. Introduction

Light detection and ranging (lidar) is a well-established remote sensing technique to measure the range of an object, using pulsed or continuous-wave lasers [1–5]. There are two main lidar ranging methods. In incoherent lidar, discrete laser pulses are sent out and the returned pulses (after interaction with a target) are collected on a detector [6]. The range is calculated from the time difference between the transmitted and received signals. The other method, coherent lidar, is based on phase sensitive (beat frequency note) detection. A continuous wave laser is amplitude (or frequency) modulated and the phase difference (or the beat frequency note) between the transmitted and return signals is used to evaluate the distance to an object. Both coherent and incoherent lidar systems are often implemented with beam scanning to enable wide coverage of an area. Lidar systems with a laser scanner can accurately generate three-dimensional (3D) measurements, beneficial to many applications. The speed of the scanners implemented in lidar systems range from 5–15 Hz for autonomous cars to 100–1000 Hz for airborne lidar applications. For instance, airborne scanning lidar can produce 3D mapping of landscapes and trees [7, 8]. Precision ranging, enabled with scanning lidar, is necessary for space station navigation (such as Mir and ISS), as well as telescope docking [9]. Other applications include navigation for self-driving cars, autonomous drones and underwater vehicles, and environmental sensing of water and snowpack. To perform a scan, lidar systems can employ mechanical or nonmechanical beam steering. Typical mechanical solutions for scanning include mirror-based gimbals, oscillating/rotating mirrors (galvanometers) [10], rotating polygons [10], rotating prisms [10, 11], and microelectromechanical systems (MEMS) mirrors [12, 13]. Nonmechanical beam steering choices include acousto-optic deflectors [14, 15], electro-optic deflectors [14, 15], liquid crystal spatial light modulators (SLM) [16–19], solid-state beam steering based on phased-arrays [20, 21], and liquid-based prisms [22–28]. Mechanical beam scanners are robust and reliable, although they commonly suffer from drawbacks such as movable parts prone to failure, large power requirements, heavy weights, large sizes, and high costs. In contrast, nonmechanical beam scanners are attractive, as they are generally low weight, compact, low power, and are often inexpensive.

One particularly attractive implementation of nonmechanical beam steering is offered by

electrowetting-based devices. Electrowetting is a mechanism in which the contact angle of a liquid droplet is modified by an external electric potential. Electrowetting-on-dielectric (EWOD) is an electrowetting phenomenon that occurs on a dielectric surface [29–33]. Recently, many studies have focused on liquid-based adaptive optical devices controlled by the EWOD principle [29–33]. The Lippmann-Young equation determines the contact angle variation with an applied electric potential,  $\cos \theta = \cos \theta_o + (\epsilon\epsilon_o)/(2\gamma d)V^2$ , where  $\theta$  is the contact angle for the applied voltage  $V$ ,  $\theta_o$  is the initial contact angle with no applied voltage,  $\epsilon$  and  $d$  are the effective dielectric constant and thickness of the dielectric layers, and  $\gamma$  is the surface tension. EWOD devices are attractive due to their large tunability, rapid response time (few ms to hundreds of ms, depending on device size and liquid combinations), low power consumption ( $< 1$  mW), transmissive nature, and lack of moving mechanical parts [29]. EWOD lenses with one electrode have been implemented in many imaging systems, such as confocal microscopy [34], miniaturized zoom lenses [35], and endoscope designs [36]. EWOD prisms (with two or more electrodes) have been used to demonstrate laser beam scanning [29–32, 37]. Lastly, multiple electrode EWOD devices have been studied to correct induced optical aberrations [38, 39]. Here, we present an implementation of a lidar system based on an EWOD prism beam scanner. To the best of our knowledge, this is the first demonstration of a lidar system integrated with a nonmechanical beam scanner based on an EWOD prism. Our design generates a  $\pm 90^\circ$  of beam steering based on  $\pm 7.8^\circ$  steering from an EWOD prism. In addition, we have designed a lidar receiver with a same field-of-view and perform a lidar scan within the laboratory environment.

## 2. Optical design and considerations

The main elements of a lidar system are the transmitter, which includes the laser source and the transmitting optics, and the receiver, which consists of optics, a detector and a data acquisition system. On the transmitter side, laser pulses with controlled divergence are sent to the target. At the receiver end, the backscattered light from the target is collected using a detector. Lidar systems can be set up in two basic configurations: monostatic and bistatic [2]. For a bistatic lidar system, the transmitter and the receiver are located at different positions (usually separated by a large distance). In a monostatic configuration, the transmitter and receiver are co-located. Monostatic configurations can be subdivided into coaxial or biaxial [2]. In the coaxial lidar arrangement, the optical axis of the transmitter coincides with the optical axis of the receiver. In the biaxial lidar layout, the optical axis of the transmitter is parallel to the receiver optical axis and are located adjacent to each other. The scanning lidar system presented in this paper is based on monostatic biaxial configuration due to its simplicity, with a separation distance of 6 cm between the transmitter and receiver.

### 2.1. Transmitter with electrowetting beam scanner

The transmitter consists of a laser source, followed by the transmitting optics such as a two-electrode EWOD prism, a Hastings achromatic triplet lens, and a miniature fisheye lens. The scanning EWOD prism, is based on a cylindrical glass tube, coated with an electrode (Indium Tin Oxide, ITO), a dielectric (Parylene HT), and a hydrophobic coating (Cytop), and epoxy bonded to an annular ground window. The device has two separated electrodes and it is filled with two immiscible liquids as shown in Figs. 1(a) and 1(b) [28]. Applying a differential AC voltage to the two electrodes alters the contact angle at the liquid-liquid interface, tilting the liquid-liquid interface; hence resulting in a tunable prism.

A brief description of the EWOD prism fabrication process is presented; more details can be found in [23, 28, 37]. A three-dimensional printed mask is placed on a cylindrical glass tube (inner diameter 3.95 mm, height 5 mm) to create separated electrodes for a two-electrode device. Next, an indium tin oxide (ITO) film (400 nm thickness) is deposited on the side wall to serve as an electrode. The 3D printed mask is removed, and the ITO electrodes are annealed at  $300^\circ\text{C}$ .

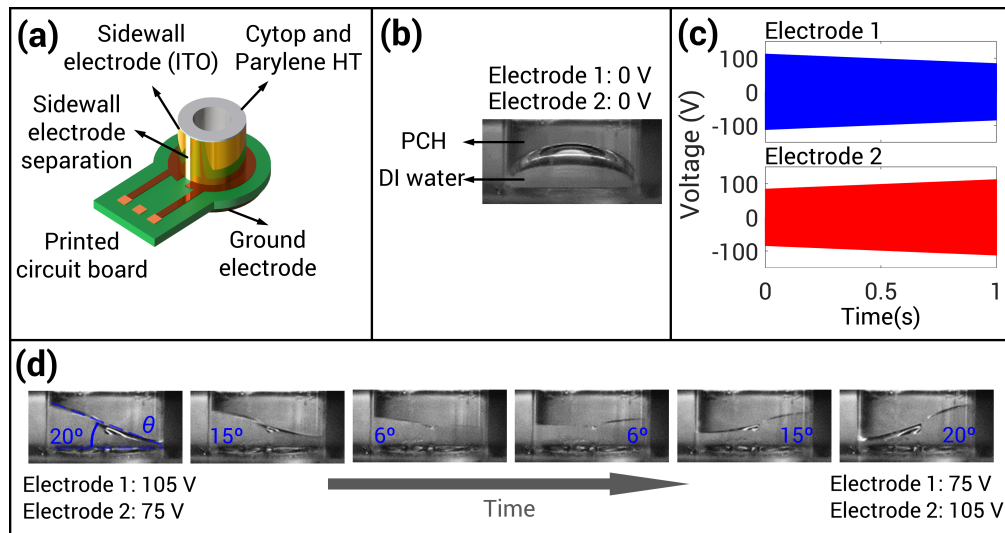


Fig. 1. (a) Schematic of the two-electrode prism device, with components labeled. The device is constructed in a cylindrical glass tube with Indium Tin Oxide (ITO) sidewall electrodes, Parylene HT as the dielectric and Cytop as the hydrophobic layer. An optical window patterned with an annular pattern of Ti/Au/Ti serves as the ground electrode. (b) An image of the two-electrode EWOD prism at initial state (0 V on both electrodes) filled with de-ionized water (DI water) and 1-Phenyl-1-cyclohexene (PCH). (c) Driving voltages with carrier frequency of 3 kHz modulated with a linear function at 1 Hz frequency between the two electrodes. (d) Series of images of the two-electrode EWOD prism, demonstrating its functionality as a tunable prism. The tilt angle of the liquid-liquid interface is labeled in each image corresponding to steering angles of 5°, 4°, and 1°, respectively.

After annealing, a 3  $\mu\text{m}$  dielectric layer of Parylene HT is deposited on top of the ITO, on the inner wall of the cylindrical glass tube. Lastly, the device is dip-coated in hydrophobic Cytop solution and cured at 185°C for 30 minutes. A glass window with annular patterned electrodes (50 nm Ti/ 300 nm Au/ 50 nm Ti) is used as the optical ground window. The optical ground window and the glass tube are epoxy bonded with an ultraviolet curable epoxy. A schematic of the assembled EWOD prism used in this work is shown in Fig. 1(a). The EWOD prism is first filled with de-ionized water (DI water,  $n = 1.33$ ) followed by 1-Phenyl-1-cyclohexene (PCH,  $n = 1.57$ ) as shown in Fig. 1(b) [28]. Our previous studies on EWOD prisms used 1 wt% sodium dodecyl sulfate (SDS) solution and dodecane. Unfortunately, this combination had a limited beam steering angle of  $\pm 2.2^\circ$  [23, 37]. With the new liquid combination of DI water and PCH, beam steering of up to  $\pm 13.7^\circ$  is possible [28].

An image of the EWOD prism filled with DI water and PCH at an initial state (0 V on both electrodes) is presented in Fig. 1(b). This liquid combination allows a large contact angle tuning of 173° to 60°, achieved by applying an AC driving voltage between 0 to 200  $V_{rms}$ . In this work, the EWOD prism (consisting of two electrodes) is actuated using a sinusoidal driving voltage with a carrier frequency of 3 kHz. The flat liquid-liquid interface (contact angle of 90°) is implemented with 95  $V_{rms}$  applied to both electrodes [28]. To perform beam steering, a differential voltage is amplitude modulated and applied to both electrodes at a set sweep frequency as plotted in Fig. 1(c). We have measured  $\pm 7.8^\circ$  of beam scanning by sweeping both electrodes with  $\pm 24 V_{rms}$  at 1 Hz around the 90° contact angle. As an example, a series of snapshots of the EWOD prism in operation are shown in Fig. 1(d) corresponding to tilt angles of 20°, 15°, and 6° at the liquid-liquid interface. This translates into beam steering angles of 5°, 4°, and 1°, respectively.

The Bond number [29] (a measure of gravitational forces compared to the surface tension) for this device is much less than unity,  $2.528 \times 10^{-5}$ , indicating that the system is dominated by surface tension forces. As a result, no ripples are generated along the liquid-liquid interface. In the dynamic scanning method presented here, the contact angle of the liquid is driven gradually with a limited tilt angle (very small contact angle change between the two electrodes during actuation). Hence, no liquid bubbles are formed through this actuation process (liquid bubbles can be generated if the device is actuated abruptly, resulting in a sudden change of the contact angles between the two electrodes). Recently, scanning speeds of up to 500 Hz were measured for a similar size EWOD prism filled with DI water and PCH. It is worth noting that the scanning range of the EWOD prism depends strongly on the modulation frequency of the driving voltage [29, 30]. If this frequency exceeds the liquid response time, the liquids cannot follow the modulation frequency resulting in a reduction of the scan range. For instance, driving an EWOD prism with 1 Hz modulation frequency with a 20 V differential voltage generates  $\pm 4.8^\circ$  of beam steering. By increasing the modulation frequency to 500 Hz with 20 V differential voltage reduces the scan angles to  $\sim \pm 0.5^\circ$  [28]. Although, the scan angles increased to  $\pm 1.74^\circ$  with an 80 V differential between the two electrodes at 500 Hz modulation frequency. The physical properties of the liquid combination, such as viscosity, and the geometrical dimensions of the device affect the frequency response of the EWOD device [29, 30].

The transmitter optical design is modeled in Zemax [40] based on the combination of the liquids (DI water and PCH) used in the EWOD prism, with a scan range of  $\pm 7.8^\circ$  around the flat meniscus (contact angle of  $90^\circ$ ). Figure 2 shows a schematic of the lidar transmitter design. To perform a nonmechanical, hemispherical scan, the steering angle from the EWOD prism must be amplified to  $\pm 90^\circ$ . For simplicity, the liquid-liquid interface of the EWOD prism is modeled as a flat interface that generates a  $\pm 7.8^\circ$  scan. A triplet lens (Thorlabs TRH127-020-A, focal length 20 mm) is added after the EWOD prism to generate a telecentric scan across the imaging circle of the miniature fisheye lens (Sunex DSL419,  $f/2$ , focal length 1.6 mm). The miniature fisheye lens is based on a sample fisheye lens from ZEBASE library (F004) and scaled down to represent the characteristics of the miniature fisheye lens used in the project (image circle 4.5 mm). The triplet lens distances are optimized for  $\pm 7.8^\circ$  of steering beam in Zemax using “RAID” and “REAY” operands. The RAID operand evaluates the ray angle of incidence on the imaging circle plane of the fisheye lens, while REAY calculates its height. Additionally, the chief ray angle of incidence is constrained to be perpendicular to the imaging circle plane to guarantee telecentricity. The miniature fisheye lens used is approximately telecentric in the image space and the triplet lens ensures that the scan stays telecentric across the image space of the fisheye lens. In addition, chief ray heights are bound to  $\pm 2.4$  mm (close to the radius of the imaging circle of the fisheye lens) to ensure a hemispherical scan of the outgoing beam from the miniature fisheye lens. Figure 2 shows the simulated spot diagrams at the imaging circle plane of the fisheye lens for different steering angles after optimization. All the spot diagrams are well within the Airy diffraction limit circle (black circle). In practice, the liquid-liquid interface of the EWOD prism exhibits a curvature that can change with actuation. The change of curvature as the prism actuates induces aberration, which is not modeled here. The liquid-liquid interface for a similar electrowetting prism (4-mm inner diameter) was modeled in [37], using computational fluid dynamics and found that an input beam diameter with FWHM larger than 1 mm has a pronounced induced aberration effect on the outgoing beam. We can reduce the induced aberration through the electrowetting prism by increasing the number of electrodes around the cylindrical tube [24]. For these reasons, we have used a collimated laser beam of 1 mm ( $1/e^2$ ) passing through electrowetting scanner to reduce the induced aberrations.

In the design presented, a triplet lens in conjunction with a wide-angle miniature fisheye lens is used to amplify the scan from an EWOD prism. Another alternative to the wide-angle miniature fisheye lens is a monocentric lens (consisting of symmetric two-glass ball lenses in the simplest

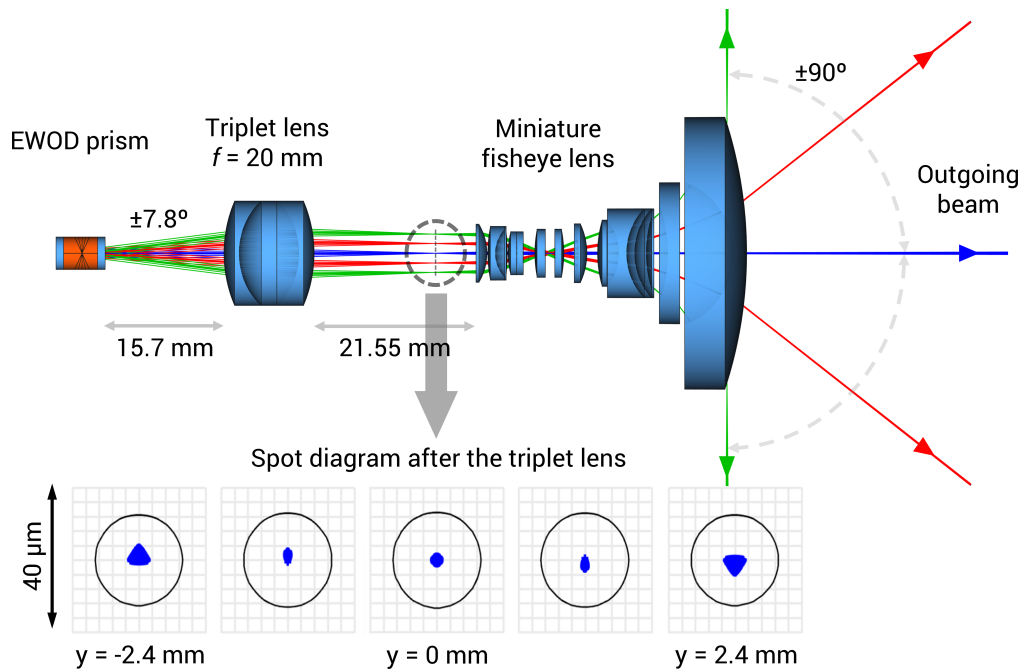


Fig. 2. Schematic optical design of the lidar transmitter modeled in Zemax for a collimated input beam width of 1 mm ( $1/e^2$ ),  $\lambda = 532$  nm. The transmitter consists of an electrowetting prism, Hastings achromatic triplet lens (Thorlabs TRH127-020-A, focal length 20 mm), and a miniature fisheye lens (Sunex DSL419,  $f/2$ , focal length 1.6 mm). The fisheye lens is adopted from ZEBASE library (F004) and scaled down to match the imaging circle of the commercially bought miniature fisheye lens (Sunex DSL419 image circle 4.5 mm). The EWOD prism produced a  $\pm 7.8^\circ$  scanning beam. Different ray colors represent five different tilts from the EWOD prism. The triple lens is used to generate a telecentric scan on the imaging circle of the fisheye lens. The spot diagram at the focal plane after the triplet lens is shown at the bottom for different scanning configurations. The spot diagrams are all well below Airy diffraction limit (black circle).

case) [41, 42], designed for wide-aperture panoramic imaging. The monocentric lens coupled with fiber bundle tapers [42] is an excellent substitute to the miniature fisheye lens and it can reduce the size of the transmitter design. However, these lenses and fiber bundle tapers are not commercially available. Thus, we choose the design described for the lidar transmitter, with commercially available components. The system is set up in the laboratory to perform detection and ranging as a proof-of-principle to showcase the utility of the liquid prism scanner.

## 2.2. Receiver optical design

The lidar receiver uses a miniature fisheye lens (same as the transmitter), two aspherical condenser lenses (Thorlabs ACL12708U and ACL25416U) and a large area ( $3 \times 3$  mm<sup>2</sup>) silicon photomultiplier (SiPM) detector. The receiver is modeled in Zemax in order to accommodate the large field-of-view of the transmitter as shown in Fig. 3. One of the challenges of the lidar receiver design for a large scanning angle transmitter is the limited size of the available detectors. For instance, the returning light from an object at  $90^\circ$  is focused off-axis on the back focal plane of the miniature fisheye lens, (see Fig. 3). The miniature fisheye lens used in this work has an image circle of 4.5 mm meaning that returning rays at large angles get focused at the edge of the imaging circle. A typical avalanche photodiode (APD) has an active area diameter of

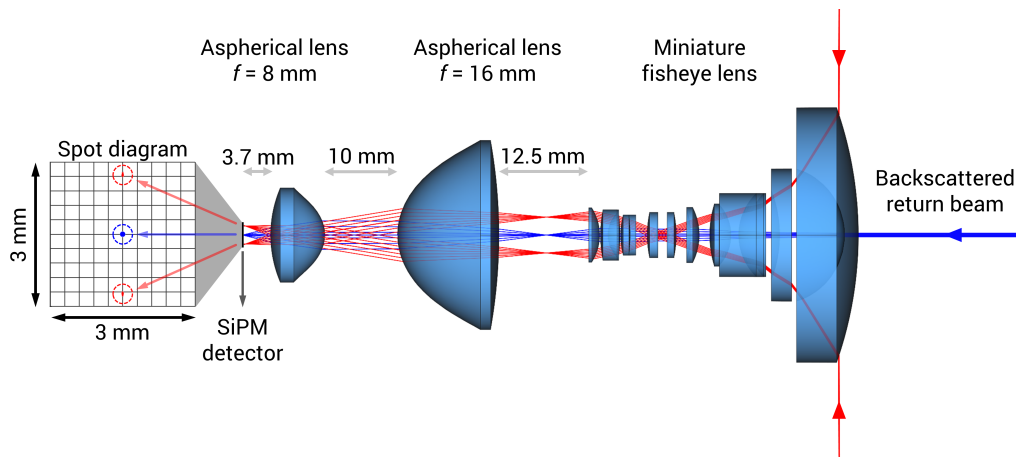


Fig. 3. Schematic optical design of the lidar receiver modeled in Zemax for backscattered return beam on axis and at  $\pm 90^\circ$ . The receiver consists of a model fisheye lens (adopted from ZEBASE library, F004), two aspherical condenser lenses (Thorlabs ACL12708U and ACL25416U) with focal lengths of 8 and 16 mm and a  $3 \times 3 \text{ mm}^2$  imaging plane as a detector (KETEK PE3325-WB-AX,  $3 \times 3 \text{ mm}^2$ ). The focal length and distance are optimized in Zemax to ensure the returning rays at large angles are focused on a  $3 \times 3 \text{ mm}^2$  plane. The spot diagrams for three different configurations are shown.

1 mm. To reduce the dimensions of the receiver, a larger active area detector based on silicon photomultiplier (SiPM) technology is selected (KETEK PE3325-WB-AX,  $3 \times 3 \text{ mm}^2$ ). SiPM detectors are composed of arrays of avalanche photodiodes operating in a Geiger mode [43]. SiPM sensors benefit from a low-light capability similar to a photomultiplier tube detector and low-voltage operation. To match the imaging circle of the fisheye lens to the detector active area, two aspherical condenser lenses are used. The receiver, using a scaled down fisheye lens and two aspherical lenses are modeled in Zemax, as shown in Fig. 3. The distance between all the elements and lenses focal lengths are optimized to guarantee the backscattered rays at large angles are collected on  $3 \times 3 \text{ mm}^2$  detector. Figure 3 depicts a spot diagram for three configurations (on-axis returning beam and returns from  $\pm 90^\circ$ ) on a  $3 \times 3 \text{ mm}^2$  detector active area.

### 3. Experimental setup

A schematic of the experimental apparatus to perform nonmechanical lidar scanning is shown in Fig. 4. The optical setup is based on the transmitter and receiver designed in Zemax described earlier. The SiPM detector used in this work has large active area of  $3 \times 3 \text{ mm}^2$  which is necessary for the current design. This detector has a photon detection efficiency of 30% at 532 nm. For this reason, a 1064 nm pulsed laser source (Teem Photonics, repetition rate 500 Hz, pulse duration  $\sim 500$  ps) is frequency doubled in a periodically poled, MgO-doped, lithium niobite in a single-pass configuration to generate 532 nm laser pulses. Two dielectric filters are used to separate the fundamental laser (1064 nm) from the second harmonic green light. 532 nm laser pulses are collimated to 1 mm ( $1/e^2$ ) using an aspheric lens and a tunable liquid lens (Optotune EL-10-30). The beam is guided into the transmitter as a laser source for the lidar experiment.

The transmitter consists of an EWOD prism, a triplet lens and a miniature fisheye lens based on the Zemax model described earlier. The distances between the optical elements in the experiment are slightly different from the Zemax model. The total distance between the EWOD prism to the back of the fisheye lens is 49.55 mm in the simulation and 60.6 mm in the experimental setup. The discrepancies are mainly caused by the EWOD prism surface profile and modeling of the

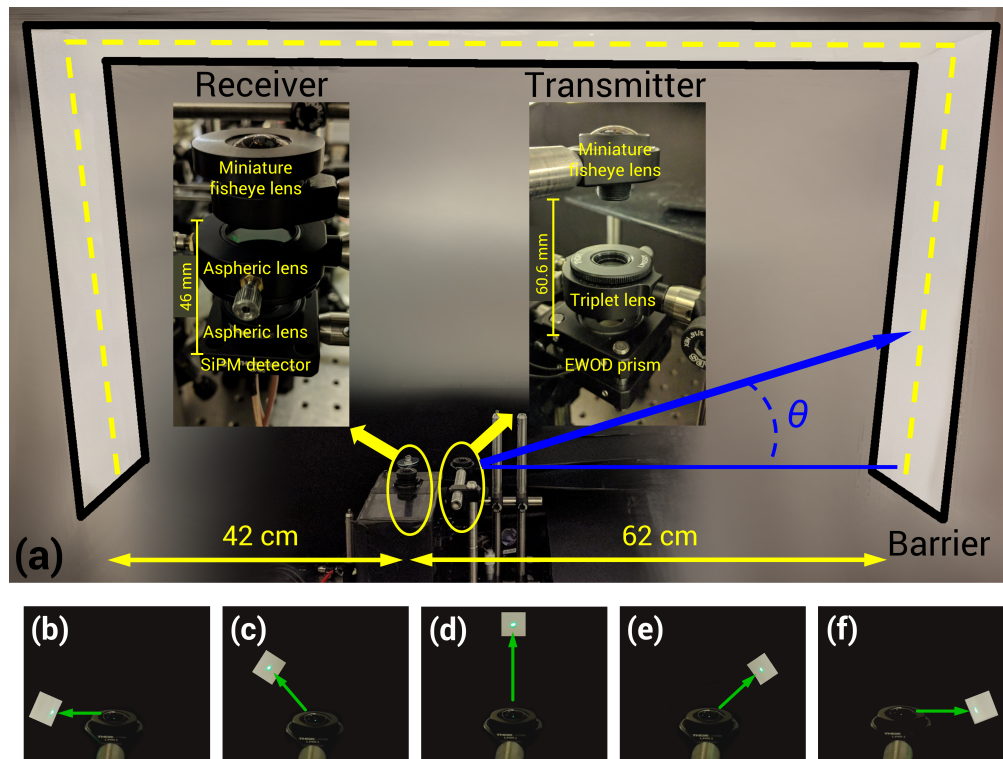


Fig. 4. (a) Lidar transmitter and receiver based on the Zemax model shown in Figs. 2 and 3. A barrier is assembled in the lab to limit the scan range as shown and highlighted by dashed lines. The insets are zoomed images of the transmitter and receiver. The distance between the optical components for the transmitter and receiver is 60.6 and 46 mm, respectively. (b)-(f) Snapshots of the outgoing beam from the transmitter scanned using EWOD prism at various steering angles. The images clearly show a  $\pm 90^\circ$  nonmechanical scan. The angle  $\theta$  represent the scanning angle originating from the right barrier.

miniature fisheye lens. For simplicity, the EWOD prism liquid-liquid interface is modeled as a flat surface that generates steering angles of  $\pm 7.8^\circ$ . In the experiment, the liquid-liquid interface exhibits a curvature (behaves as a lens) at the operating voltages that alter the divergence of the beam. To compensate for this beam divergence, the distances between the optical elements are adjusted in the experiment. In addition, the fisheye lens used in the Zemax model (from ZEBASE library) does not exactly represent the one implemented in the experiment. These are the main reasons for the difference between the simulations and the experiment. The receiver is assembled, based on the Zemax model, with the addition of a bandpass filter to remove ambient background light. Figures 4(b) to 4(f) shows snapshot images of the lidar transmitter at various scanning angles.

In addition, optical leakage from the outgoing laser pulse is recorded by an APD (Thorlabs APD430A) and directed into a two-channel constant fraction discriminator (CFD, SensL HRM-CFD). The CFD output signals are used to provide the start signal to a time-digital converter (TDC, SensL HRM-TDC). The scattered light from the target is collected by the receiver and amplified. The amplified output of the SiPM is input to the second channel of the CFD. Each CFD output signal is passed to the TDC, operating with a 27-ps bin width [44] (equivalent of  $\pm 4$  mm range, with integration time 1s or 500 shots). Time-of-flight (TOF) measurements are calculated by differencing the start time sampled by the APD and the signal received (stop signal)

from the SiPM detector.

#### 4. Results and discussion

To test the lidar, a simple nonmechanical scan is performed within the laboratory environment. The actual environment is shown as the barricade in Fig. 4(a). Figure 5(a) shows a one-dimensional measured distance using an EWOD prism. The scan in Fig. 5(a) plots the relative received signal (converted to distance in cm) as a function of scanning angle of the transmitter. The scan, initiated from the right side of the barricade in Fig. 4(a), corresponds to a scan angle of zero degrees, labeled as  $\theta$ . The scan is continuous, using a sinusoidal driving voltage (carrier frequency of 3 kHz and amplitude of 100 V) modulated with a linear sweeping function (frequency of 0.05 Hz, and amplitude of  $\pm 24$  V). The given input voltage translates into an EWOD prism scan of  $\pm 7.8^\circ$ , which is magnified to  $\pm 90^\circ$  with the transmitter design. The EWOD scanner with a 1-mm diameter beam generates  $\sim 500$  resolvable spots for  $\pm 7.8^\circ$  scanning at 1 Hz, defined by the ratio of total scan angle to the beam divergence [45]. The divergence of the outgoing beam is measured to be 6 mrad and results in a  $\sim 6$  cm beam diameter at a 10-meter distance.

Two cusp-shaped features in the graph correspond to the corners of the barricade as the distance increases and decreases, while scanning through these corners. The polar scan data is transformed to Cartesian coordinates, as shown in Fig. 5(b). The Cartesian coordinates represent the shape of the physical barricade in the laboratory environment. The scan has been repeated for various sweeping frequencies ranging from 0.05 to 2 Hz. The transmitter scan range of  $\pm 90^\circ$  is unaltered for all of these sweep frequencies. Increasing the sweeping frequency above 2 Hz results in a decrease of the scanning angle. This is mainly attributed to the frequency response of the liquids in the given device geometry [28–30]. At higher frequencies, the liquids cannot respond fully to the applied voltage resulting in a limited scan range [28]. However, increasing the amplitude of the driving voltage at higher scan frequencies can enhance the steering angles further [28]. The response time of electrowetting devices can be described by,  $\tau \propto \sqrt{\rho D^3 / \gamma}$ , where  $\rho$  is the fluid density,  $D$  is the aperture size, and  $\gamma$  is the interfacial tension [46]. Hence, reducing the dimension of the EWOD prism can significantly enhance the scanning speed. In addition to the device size, the viscosity of the liquids and the shape of the driving voltage affect the electrowetting response time [47–49]. Recent advances allow fabrication of electrowetting microlens and microprism arrays with operation frequencies in the kHz range [50, 51]. Using microprism arrays allow for fast scanning speeds which makes this technology comparable to the current mechanical scanner used in lidar systems.

Another important consideration for a lidar system is the laser average and peak powers, determining the maximum system range. Typical commercial lidar systems used in autonomous cars are based on tens of mW average power (repetition rate  $\sim 30$  kHz, pulse duration 5 ns, peak power 60 W,  $\lambda = 903$  nm) for range measurements  $< 100$  meters [52]. Recently, a two-electrode electrowetting prism was implemented in a two-photon microscopy system [37]. The component was used with a laser system that had a peak power of a few kW (repetition rate  $\sim 80$  MHz, pulse duration 90 fs, average power  $\sim 80$  mW,  $\lambda = 950$  nm), making it an attractive choice for scanning lidar ranges  $< 100$  m, in which the power requirements can be satisfied with an electrowetting prism scanner.

The typical operating wavelength for many lidar systems is 905 nm. The 532 nm source used in this work is chosen for experimental convenience. Again, the choice of wavelength will be determined by the application. For instance, a polarization lidar system for shallow water depth measurement was implemented at 532 nm [53], while autonomous cars often use lidar at 905 nm. The liquid combination (DI water and PCH) used in the electrowetting scanner is transmissive at these wavelengths (532 and 905 nm). At longer wavelengths ( $> 1 \mu\text{m}$ ), DI water absorption increases with a peak around 1.4–1.5  $\mu\text{m}$ . To design a lidar system at longer wavelength ( $> 1 \mu\text{m}$ ) based on an electrowetting scanner, ionic liquids and liquid metals can be implemented [54, 55].

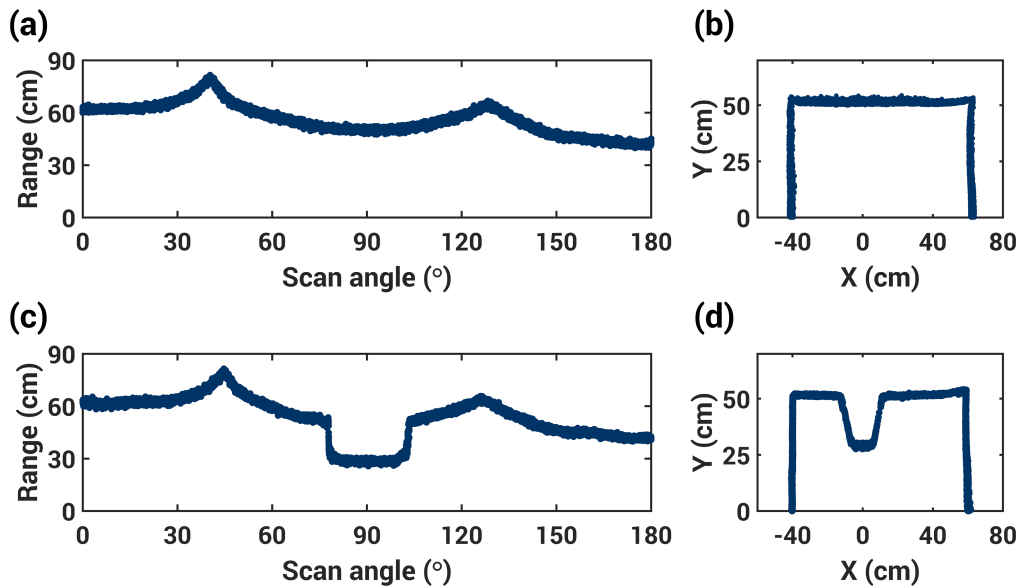


Fig. 5. (a) The measured range as a function of scan angle (nonmechanical beam scanning with EWOD prism) within a laboratory environment. (b) The lidar data presented in (a) is transformed to Cartesian coordinates. The distance from the transmitter to the barricade is accurately measured using the nonmechanical beam scanner. For instance, the range value at  $0^\circ$  and  $180^\circ$ , corresponds to the left and right barricade positions, respectively. (c) The measured ranges as a function of scan angle with an extra obstacle introduced in the scanning path. (d) The lidar data presented in (c) is transformed to Cartesian coordinates. The obstacle with the width of 20 cm is clearly measured at  $90^\circ$  scan angle with the range value of 30 cm.

In the second example, an obstacle (width 20 cm) is introduced into the scanning path of the transmitter and receiver. The return signal is converted to the distance and plotted in Fig. 5(c) as a function of scanning angle. The measured distance is reduced to 30 cm as the transmitter passes through the added obstacle at  $90^\circ$ . In a similar manner the distance measurement is transformed to Cartesian coordinates (see Fig. 5(d)). To the best of our knowledge, this is the first demonstration of a lidar system with a nonmechanical beam scanner based on an EWOD prism. The compactness and simplicity of the transmitter optical design is mainly due to the large tuning angle acquired by the EWOD prism in conjunction with a miniature wide-angle lens.

The current proof-of-principle lidar design demonstrates the viability of nonmechanical beam scanning lidar based on EWOD prism. Two-dimensional lidar scanning is also possible by replacing the two-electrode EWOD prism with a four or more electrode EWOD device in the same optical design. A four-electrode EWOD prism can be fabricated through the same process described here and generates tilts at two perpendicular directions, making it ideal as a two-dimensional tunable prism. Recently, eight and sixteen-electrode devices were fabricated to demonstrate aberration corrections and two-dimensional beam steering [24, 38].

## 5. Conclusion

We have designed and constructed a benchtop lidar transmitter and receiver based on a two-electrode EWOD prism. The EWOD prism is filled with DI-water and PCH liquids, enabling  $\pm 7.8^\circ$  of scanning with a single prism device. A Zemax model is generated to integrate the EWOD prism in a lidar transmitter to perform a hemispherical scan of  $\pm 90^\circ$ . The optical design

of a lidar receiver is presented, showing a method to collect return backscattered light at large angles. A proof-of-principle lidar system is constructed based on the simulation results within the laboratory environment. Range measurements with the laboratory environment are presented using EWOD prism scanner in the lidar transmitter. The results show that we can easily send and receive light pulses at large angles. Two dimensional lidar scanning can be performed by replacing the two-electrode EWOD prism with a four-electrode EWOD prism. An optical system based on a EWOD prism scanner has great potential for many applications in addition to lidar, such as compact laser projection display, laser surgery, medical imaging, endoscopic imaging, microscopy, autonomous control, and machine vision.

## Funding

Office of Naval Research (ONR) (N00014-15-1-2739); National Science Foundation (NSF) Instrument Development for Biological Research (IDBR) (DBI-1353757) and Chemical, Bioengineering, Environmental and Transport Systems (CBET-1631704); National Institutes of Health Stimulating Peripheral Activity to Relieve Conditions (SPARC) (OT2OD023852) and Brain Research through Advancing Innovative Neurotechnologies (BRAIN) (U01 NS099577-02).

## Acknowledgments

The authors would like to acknowledge Rory Barton-Grimley and Prof. Jeffrey Thayer (Univ. of Colorado Boulder) for the loan and assistance with the data acquisition of the lidar system. Publication of this chapter was funded by the University of Colorado Boulder Libraries Open Access Fund.

## References

1. R. T. H. Collis, "Lidar," *Appl. Opt.* **9**, 1782–1788 (1970).
2. R. G. Driggers, *Encyclopedia of Optical Engineering - Volume 2* (CRC, 2003).
3. C. G. Bachman, *Laser Radar Systems and Techniques* (Artech House, 1979).
4. G. W. Kattawar and G. N. Plass, "Time of flight lidar measurements as an ocean probe," *Appl. Opt.* **11**, 662–666 (1972).
5. J. W. Hair, C. A. Hostetler, A. L. Cook, D. B. Harper, R. A. Ferrare, T. L. Mack, W. Welch, L. R. Izquierdo, and F. E. Hovis, "Airborne high spectral resolution lidar for profiling aerosol optical properties," *Appl. Opt.* **47**, 6734–6752 (2008).
6. R. D. Richmond and S. C. Cain, *Direct-Detection LADAR Systems* (SPIE, 2010).
7. M. A. Lefsky, W. B. Cohen, G. G. Parker, and D. J. Harding, "Lidar remote sensing for ecosystem studies," *BioScience* **52**, 19–30 (2002).
8. E. Næsset, T. Gobakken, J. Holmgren, H. Hyypä, J. Hyypä, M. Maltamo, M. Nilsson, H. Olsson, Å. Persson, and U. Söderman, "Laser scanning of forest resources: the nordic experience," *Scand. J. For. Res.* **19**, 482–499 (2004).
9. J. L. Goodman, "History of space shuttle rendezvous and proximity operations," *J. Spacecr. Rockets* **43**, 944–959 (2006).
10. A. Wehr and U. Lohr, "Airborne laser scanning—an introduction and overview," *ISPRS J. Photogramm. Remote Sens.* **54**, 68–82 (1999).
11. B. D. Duncan, J. B. Philip, and S. Vassili, "Wide angle achromatic prism beam steering for infrared countermeasure applications," *Opt. Eng.* **42**, 1038–1047 (2003).
12. M. G. da Silva, D. W. DeRoo, M. J. Tracy, A. Rybaltowski, C. G. Caffisch, and R. M. Potenza, "Ladar using mems scanning," US Patent 20120236379 A1 (2012).
13. U. Hofmann, J. Janes, and H. Quenzer, "High-q mems resonators for laser beam scanning displays," *Micromachines* **3**, 509–528 (2012).
14. G. Römer and P. Bechtold, "Electro-optic and acousto-optic laser beam scanners," *Phys. Procedia* **56**, 29–39 (2014).
15. S. R. Davis, G. Farca, S. D. Rommel, A. W. Martin, and M. H. Anderson, "Analog, non-mechanical beam-steerer with 80 degree field of regard," *Proc. SPIE* **6971**, 69710G1 (2008).
16. D. P. Resler, D. S. Hobbs, R. C. Sharp, L. J. Friedman, and T. A. Dorschner, "High-efficiency liquid-crystal optical phased-array beam steering," *Opt. Lett.* **21**, 689–691 (1996).
17. J. Kim, C. Oh, M. J. Escuti, L. Hosting, and S. Serati, "Wide-angle nonmechanical beam steering using thin liquid crystal polarization gratings," *Proc. SPIE* **7093**, 709302 (2008).

18. J. Lindle, A. Watnik, and V. Cassella, "Efficient multibeam large-angle nonmechanical laser beam steering from computer-generated holograms rendered on a liquid crystal spatial light modulator," *Appl. Opt.* **55**, 4336–4341 (2016).
19. E. J. Haellstig, L. Sjoqvist, and M. Lindgren, "Intensity variations using a quantized spatial light modulator for nonmechanical beam steering," *Opt. Eng.* **42**, 612–619 (2003).
20. J. K. Doyle, M. J. R. Heck, J. T. Bovington, J. D. Peters, L. A. Coldren, and J. E. Bowers, "Two-dimensional free-space beam steering with an optical phased array on silicon-on-insulator," *Opt. Express* **19**, 21595–21604 (2011).
21. C. V. Poulton, A. Yaacobi, D. B. Cole, M. J. Byrd, M. Raval, D. Vermeulen, and M. R. Watts, "Coherent solid-state lidar with silicon photonic optical phased arrays," *Opt. Lett.* **42**, 4091–4094 (2017).
22. N. R. Smith, D. C. Abeysinghe, J. W. Haus, and J. Heikenfeld, "Agile wide-angle beam steering with electrowetting micropisms," *Opt. Express* **14**, 6557–6563 (2006).
23. S. Terrab, A. M. Watson, C. Roath, J. T. Gopinath, and V. M. Bright, "Adaptive electrowetting lens-prism element," *Opt. Express* **23**, 25838–25845 (2015).
24. D. Kopp, L. Lehmann, and H. Zappe, "Optofluidic laser scanner based on a rotating liquid prism," *Appl. Opt.* **55**, 2136–2142 (2016).
25. L. L. C. Liu and Q.-H. Wang, "Liquid prism for beam tracking and steering," *Opt. Eng.* **51**, 114002 (2012).
26. J. Cheng and C.-L. Chen, "Adaptive beam tracking and steering via electrowetting-controlled liquid prism," *Appl. Phys. Lett.* **99**, 191108 (2011).
27. C. E. Clement and S.-Y. Park, "High-performance beam steering using electrowetting-driven liquid prism fabricated by a simple dip-coating method," *Appl. Phys. Lett.* **108**, 191601 (2016).
28. W. Y. Lim, O. Supekar, M. Zohrabi, J. Gopinath, and V. Bright, "A liquid combination with high refractive index contrast and fast scanning speeds for electrowetting adaptive optics," *Langmuir* **34**, 14511–14518 (2018).
29. F. Mugele and J. Baret, "Electrowetting: from basics to applications," *J. Phys. Condens. Matter* **17**, R705–R774 (2005).
30. J. C. Baret, M. M. J. Decré, and F. Mugele, "Self-excited drop oscillations in electrowetting," *Langmuir* **23**, 5173–5179 (2007).
31. B. Berge and J. Peseux, "Variable focal lens controlled by an external voltage: An application of electrowetting," *Eur. Phys. J. E* **3**, 159–163 (2000).
32. H. Ren and S.-T. Wu, *Introduction to Adaptive Lenses* (John Wiley and Sons, Inc., 2012).
33. B. H. W. Hendriks, S. Kuiper, M. A. J. V. As, C. A. Renders, and T. W. Tukker, "Electrowetting-based variable-focus lens for miniature systems," *Opt. Rev.* **12**, 255–259 (2005).
34. B. N. Ozbay, J. T. Losacco, R. Cormack, R. Weir, V. M. Bright, J. T. Gopinath, D. Restrepo, and E. A. Gibson, "Miniaturized fiber-coupled confocal fluorescence microscope with an electrowetting variable focus lens using no moving parts," *Opt. Lett.* **40**, 2553–2556 (2015).
35. Y. Fang, C. Tsai, and C. Chung, "A study of optical design and optimization of zoom optics with liquid lenses through modified genetic algorithm," *Opt. Express* **19**, 16291–16302 (2011).
36. M. E. Pawlowski, S. Shrestha, J. Park, B. E. Applegate, J. S. Oghalai, and T. S. Tkaczyk, "Miniature, minimally invasive, tunable endoscope for investigation of the middle ear," *Biomed. Opt. Express* **6**, 2246–2257 (2015).
37. O. D. Supekar, B. N. Ozbay, M. Zohrabi, P. D. Nystrom, G. L. Futia, D. Restrepo, E. A. Gibson, J. T. Gopinath, and V. M. Bright, "Two-photon laser scanning microscopy with electrowetting-based prism scanning," *Biomed. Opt. Express* **8**, 5412–5426 (2017).
38. D. Kopp and H. Zappe, "Tubular astigmatism-tunable fluidic lens," *Opt. Lett.* **41**, 2735–2738 (2016).
39. M. Zohrabi, R. H. Cormack, C. McCullough, O. D. Supekar, E. A. Gibson, V. M. Bright, and J. T. Gopinath, "Numerical analysis of wavefront aberration correction using multielectrode electrowetting-based devices," *Opt. Express* **25**, 31451–31461 (2017).
40. Radiant ZEMAX, *Optical Design Program, User's Manual* (2018).
41. I. A. I. Stamenov and J. E. Ford, "Optimization of high-performance monocentric lenses," *Appl. Opt.* **52**, 8287–8304 (2013).
42. S. Karbasi, I. Stamenov, N. Motamedi, A. Arianpour, A. R. Johnson, R. A. Stack, C. LaReau, R. Tenill, R. Morrison, I. P. Agurok, and J. E. Ford, "Curved fiber bundles for monocentric lens imaging," *Proc. SPIE* **9579**, 95790G (2015).
43. C. Degenhardt, G. Prescher, T. Frach, A. Thon, R. de Gruyter, A. Schmitz, and R. Ballizany, "The digital silicon photomultiplier — a novel sensor for the detection of scintillation light," in *Proceedings of IEEE Nuclear Science Symposium and Medical Imaging Conference (NSS/MIC)*, (IEEE, 2009), pp. 2383–2386.
44. S. E. Mitchell and J. P. Thayer, "Ranging through shallow semitransparent media with polarization lidar," *J. Atmospheric Ocean. Technol.* **31**, 681–697 (2014).
45. P. R. Patterson, D. Hah, M. Fujino, W. Piyawattanametha, and M. C. Wu, "Scanning micromirrors: an overview," *Proc. SPIE* **5604**, 560413 (2004).
46. S. Kuiper and B. H. W. Hendriks, "Variable-focus liquid lens for miniature cameras," *Appl. Phys. Lett.* **85**, 1128–1130 (2004).
47. J. Hong, Y. K. Kim, K. H. Kang, J. M. Oh, and I. S. Kang, "Effects of drop size and viscosity on spreading dynamics in dc electrowetting," *Langmuir* **29**, 9118–9125 (2013).
48. J. B. Chae, J. Hong, S. J. Lee, and S. K. Chung, "Enhancement of response speed of viscous fluids using overdrive voltage," *Sens. Actuators* **209**, 56–60 (2015).

49. O. D. Supekar, M. Zohrabi, J. T. Gopinath, and V. M. Bright, "Enhanced response time of electrowetting lenses with shaped input voltage functions," *Langmuir* **33**, 4863–4869 (2017).
50. C. U. Murade, D. van der Ende, and F. Mugele, "High speed adaptive liquid microlens array," *Opt. Express* **20**, 18180–18187 (2012).
51. L. Hou, J. Zhang, N. Smith, J. Yang, and J. Heikenfeld, "A full description of a scalable microfabrication process for arrayed electrowetting microprisms," *J. Micromechanics Microengineering* **20**, 015044 (2010).
52. Velodyne LiDAR, *Velodyne Lidar HDL-64E Manual*.
53. S. Mitchell, J. P. Thayer, and M. Hayman, "Polarization lidar for shallow water depth measurement," *Appl. Opt.* **49**, 6995–7000 (2010).
54. P. Sen and C. Kim, "A fast liquid-metal droplet microswitch using ewod-driven contact-line sliding," *J. Microelectromech. Syst.* **18**, 174–185 (2009).
55. S. Millefiorini, A. H. Tkaczyk, R. Sedev, J. Efthimiadis, and J. Ralston, "Electrowetting of ionic liquids," *J. Am. Chem. Soc.* **128**, 3098–3101 (2006).